Author/s:
Berkman, IR;Lyasota, A;de Boo, GG;Bartholomew, JG;Lim, SQ;Johnson, BC;McCallum, JC;Xu, BB;Xie, S;Abrosimov, NV;Pohl, HJ;Ahlefeldt, RL;Sellars, MJ;Yin, C;Rogge, S

Title:
Long optical and electron spin coherence times for erbium ions in silicon

Date:
2025-12-01

Citation:
Berkman, I. R., Lyasota, A., de Boo, G. G., Bartholomew, J. G., Lim, S. Q., Johnson, B. C., McCallum, J. C., Xu, B. B., Xie, S., Abrosimov, N. V., Pohl, H. J., Ahlefeldt, R. L., Sellars, M. J., Yin, C. & Rogge, S. (2025). Long optical and electron spin coherence times for erbium ions in silicon. Npj Quantum Information, 11 (1), pp.66-. https://doi.org/10.1038/s41534-025-01008-x.

Persistent Link:
https://hdl.handle.net/11343/363377

npj | quantum information

Article

Published in partnership with The University of New South Wales

https://doi.org/10.1038/s41534-025-01008-x

Long optical and electron spin coherence times for erbium ions in silicon

Ian R. Berkman[1,10], Alexey Lyasota[1,10], Gabriele G. de Boo[1], John G. Bartholomew[2,3], Shao Qi Lim[4], Brett C. Johnson[4,5], Jeffrey C. McCallum[4], Bin-Bin Xu[1], Shouyi Xie[1], Nikolay V. Abrosimov[6], Hans-Joachim Pohl[7], Rose L. Ahlefeldt[8], Matthew J. Sellars[8], Chunming Yin[1,9] & Sven Rogge[1] ✉

Spins in silicon that are accessible via a telecom-compatible optical transition are a versatile platform for quantum information processing that can leverage the well-established silicon nanofabrication industry. Key to these applications are long coherence times on the optical and spin transitions to provide a robust system for interfacing photonic and spin qubits. Here, we report telecom-compatible Er^{3+} sites with long optical and electron spin coherence times, measured within a nuclear spin-free silicon crystal (<0.01 % ^{29}Si) using optical detection. We investigate two sites and find 0.1 GHz optical inhomogeneous linewidths and homogeneous linewidths below 70 kHz for both sites. We measure the electron spin coherence time of both sites using optically detected magnetic resonance and observe Hahn echo decay constants of 0.8 ms and 1.2 ms at ~ 11 mT. These optical and spin properties of Er^{3+}:Si are an important milestone towards using optically accessible spins in silicon for a broad range of quantum information processing applications.

Quantum information processing (QIP) offers numerous protocols that outperform equivalent classical protocols in terms of computational speed and security[1–11]. In order to enact these protocols, the ability to coherently manipulate and entangle multiple quantum states is required. Electron spins in silicon are attractive qubits due to the fast control of the highly coherent spin states[12–23] and the ability to use well-established semiconductor processing techniques to fabricate scalable nanometer architectures with high yield[24–28]. Additionally, silicon systems that are capable of photon-mediated spin-spin coupling are promising candidates for inter-chip and chip-to-chip coupling in quantum computing[29–32], and for long-distance coupling in quantum networks[4,33–35]. For these spin-photon systems, it is favourable to minimise the photon losses between the spin qubits in order to achieve entanglement operations with high fidelity and efficiency.

Among the lowest loss architectures currently available is the combination of telecommunication band photons with silicon photonics[36]. Not only are silicon devices at the forefront of high performance photonic integration, but they also lead the technologically important complementary metal-oxide-semiconductor (CMOS) field. These mature silicon industries can be leveraged to realise very large-scale integration (VLSI) photonic circuits by using on-chip silicon-based components such as ultra-high quality factor cavities[37], low-loss waveguides[38], phase-shifters[39,40], modulators[41] and near-unity single photon detectors[40]. For these reasons, realising telecom-wavelength emitters in silicon for QIP applications is a highly active area of research, with artificial atoms showing remarkable progress as optically active centres[23,42–47].

Realising a high performance spin-photon interface imposes two additional requirements on optically active centres in silicon: long electron spin coherence times and long optical coherence times[33,48,49]. For this purpose, Er^{3+} ions are strong candidates. Er^{3+} ions possess an electrically shielded intra-shell optical transition with emission in the lowest loss telecommunication C-band and an effective spin-1/2 ground electron spin state transition. Important QIP milestones have been achieved using Er^{3+} ions in insulator host crystals. For example, Er^{3+} ensembles in Y_2SiO_5 exhibit optical linewidths down to 73 Hz in large magnetic fields[50], and nuclear spin

[1]Centre of Excellence for Quantum Computation and Communication Technology, School of Physics, University of New South Wales, Sydney, NSW, 2052, Australia. [2]Centre for Engineered Quantum Systems, School of Physics, The University of Sydney, Sydney, NSW, 2006, Australia. [3]The University of Sydney Nano Institute, The University of Sydney, Sydney, NSW, 2006, Australia. [4]Centre of Excellence for Quantum Computation and Communication Technology, School of Physics, University of Melbourne, Melbourne, VIC, 3010, Australia. [5]School of Science, RMIT University, Melbourne, VIC, 3001, Australia. [6]Leibniz-Institut für Kristallzüchtung, 12489 Berlin, Germany. [7]VITCON Projectconsult GmbH, 07745 Jena, Germany. [8]Centre of Excellence for Quantum Computation and Communication Technology, Research School of Physics, Australian National University, Canberra, ACT, 0200, Australia. [9]CAS Key Laboratory of Microscale Magnetic Resonance and School of Physical Sciences, University of Science and Technology of China, Hefei, 230026, China. [10]These authors contributed equally: Ian R. Berkman, Alexey Lyasota ✉e-mail: s.rogge@unsw.edu.au

coherence times of over one second[51]. Furthermore, ground state electron spin coherence times of up to 23 ms have been measured in Er^{3+}:$CaWO_4$[52]. Er^{3+} ensembles have also been used to demonstrate prototype microwave-to-optical transducers[53–55], including integrated on-chip geometries[56].

At a single ion level, Er^{3+} ions in $CaWO_4$ have demonstrated indistinguishable single photon emission at telecommunication wavelengths[57], enabled by 150 kHz optical linewidths and 12-h long spectral diffusion of 63 kHz. In addition, this study achieved >97% single-shot readout fidelity optical quantum non-demolition measurements, similar to observations in Er^{3+}:Y_2SiO_5[58]. By embedding Er^{3+} ions in $LiNbO_3$, the emission of single ions can also be controlled[59]. Finally, the large gyromagnetic moment of the Er^{3+} electron spin has enabled single electron spin resonance (ESR) detection[60].

Despite the individual appeal of both silicon as a host material platform and Er^{3+} ions as a spin-photon interface, Er^{3+}:Si systems have not yet demonstrated comparable performance to Er^{3+} ions in the solid-state materials mentioned above. While the optical properties of Er^{3+}:Si systems have been studied, resulting in the observation of sub-megahertz homogeneous linewidths[61,62], there are few studies on the Er^{3+} electron spin transition in silicon. To date, the Er^{3+}:Si electron spin coherence time has solely been measured using bulk ESR, demonstrating a $T_{2,\mathrm{Hahn}}$ of 7.5 µs in natural silicon, which is likely limited by superhyperfine coupling to ^{29}Si spins[63]. Realising long Er^{3+}:Si electron spin coherence times on optically active sites has therefore remained elusive.

In order for Er^{3+}:Si to be deemed suitable for QIP applications, we quantify the important properties that have to be met for an Er^{3+}:Si site. First, the site should be optically active and exhibit narrow homogeneous linewidths to enable high cooperativity coupling to nanophotonic cavities. Cooperativity is given by the Purcell enhanced lifetime over the homogeneous linewidth. Effective Purcell enhancements of over 650 are routinely observed for Er^{3+} ions in other host materials evanescently coupled to Si nanophotonic cavities[57,64]. For Er^{3+}:Si nanophotonics cavities, the Er^{3+} ions reside within the cavities, leading to a promising avenue for larger Purcell enhancement. We can hence assume that Purcell enhancements of 1000 are

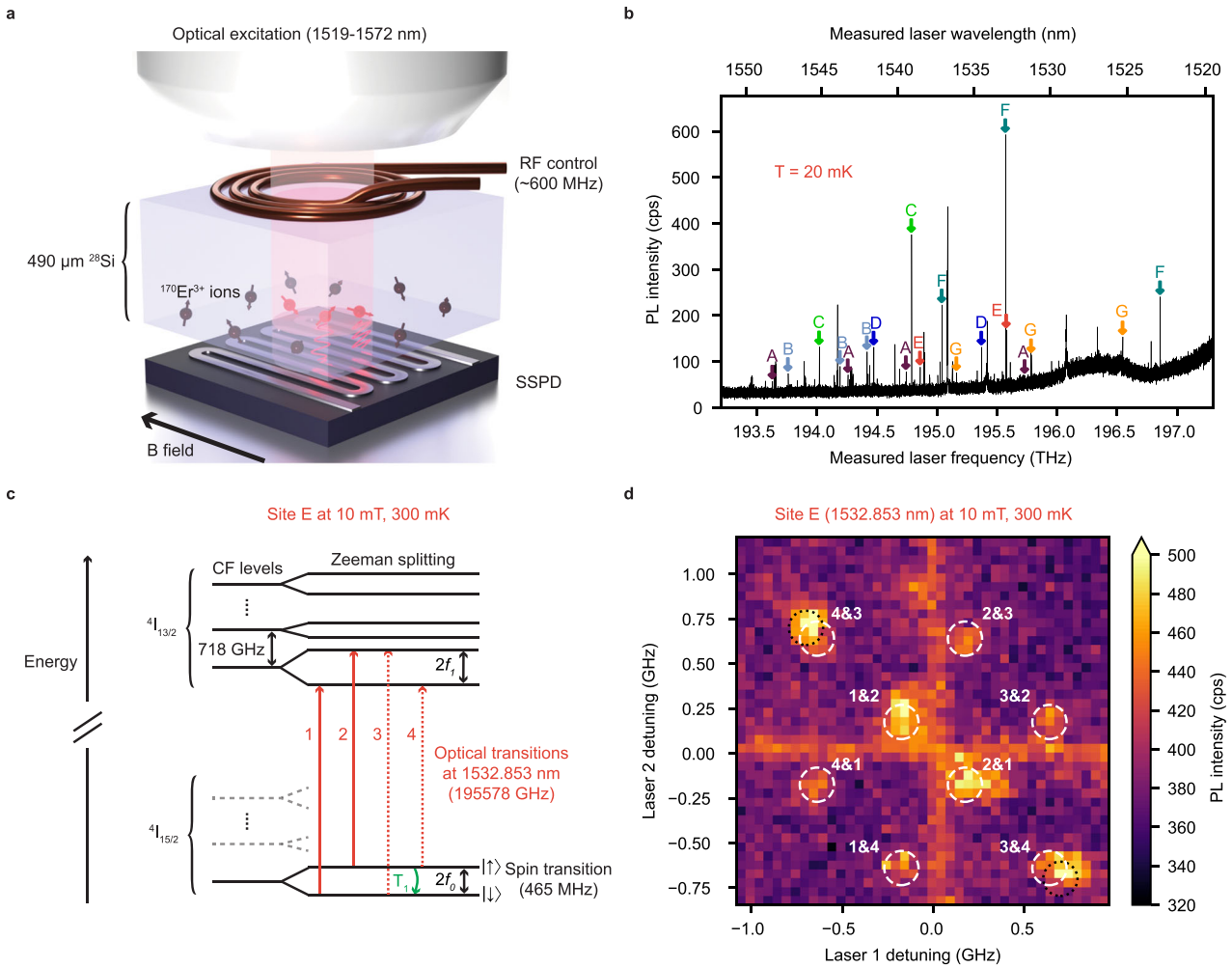

Fig. 1 | Photoluminescent excitation spectrum of Er^{3+} ions in silicon. a Schematic of the setup to perform photoluminescence excitation (PLE) and optically detected magnetic resonance (ODMR) spectroscopy of Er^{3+} ions in silicon. The optical excitation consists of a laser pulse which excites the Er^{3+} ions resonant with the laser. Directly after the pulse, the photoluminescence (PL) of these Er^{3+} ions are collected by a superconducting single-photon detector (SSPD). The antenna consists of a copper wire and is solely used for the ODMR measurements. **b** PLE spectrum of the Er^{3+} ions in ^{28}Si. The letters denote the different sites observed and the resonances that belong to the same site. **c** Energy level diagram of Site E under 10 mT. The optical transition is excited using the laser light, whereas the spin transition is controlled using the RF antenna in (**a**). The values in this diagram are extracted from the PLE spectrum in (**a**), as well as the Zeeman spectrum in (**d**). The solid red lines refer to spin-conserving transitions, while the dashed red lines refer to spin-flipping transitions. **d** 2D Zeeman spectrum, showing a recovery (dashed circles) of the signal solely when the two lasers excite from both of the ground electron spin states as displayed in (**c**). The numbers next to each recovered signal correspond, respectively, to the first and second laser, and the transitions excited in (**c**). The detuned frequencies where the Zeeman signals are observed occur at $\pm(f_1 - f_0) = \pm 175$ MHz and $\pm(f_0 + f_1) = \pm 640$ MHz. An additional Er^{3+} orientation is visible with $f_0 = f_1 = 350$ MHz, displayed by the bright horizontal and vertical line, and the bright signal close to transitions 4& 3 (3& 4), indicated with the black dashed circles.

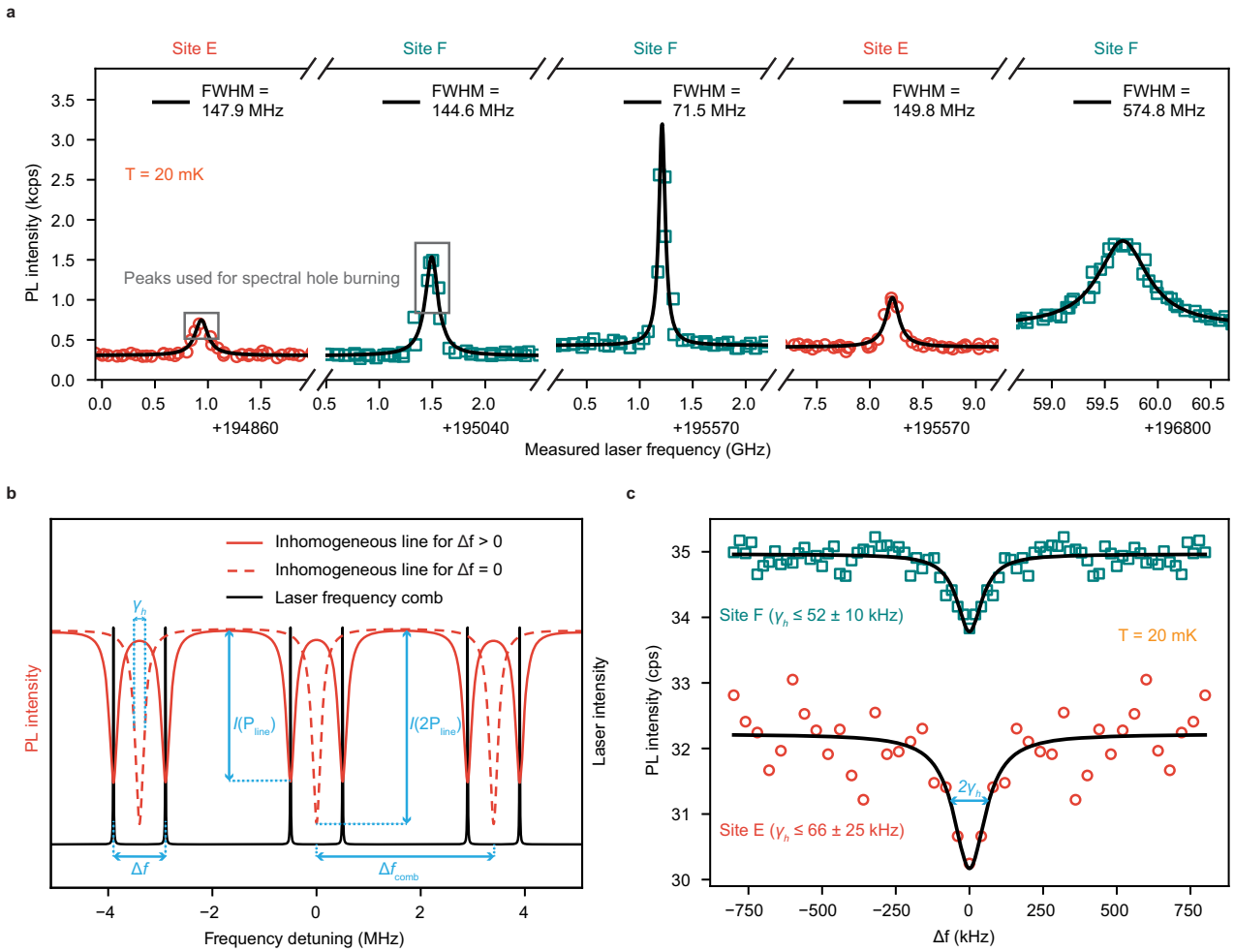

Fig. 2 | Optical transition properties of Site E and Site F. a Photoluminescence excitation (PLE) spectrum of Site E and Site F, fit with a Lorentzian distribution to extract the inhomogeneous linewidths, showing narrow linewidths for the sites. **b** Schematic of the spectral hole burning technique to extract the upper bound on the homogeneous linewidth (γ_h). For Site E and Site F, a frequency comb of $N_{doublet} = 18$ doublets is used, with a Δf_{comb} of 3.4 MHz. P_{sb} refers to the optical power on the sample for each sideband. At $\Delta f_{doublet} = 0$, N spectral holes are burned, whereas for $\Delta f_{doublet} > \gamma_h$, $2N$ spectral holes are burned. Because of atomic saturation, the PL intensity increases for increasing values of $\Delta f_{doublet}$, allowing the extraction of the upper bound on γ_h. **c** PL intensity as a function of $\Delta f_{doublet}$ for Site E (P_{sb} = 139 nW) and Site F (P_{sb} = 35 nW). The resulting spectral holes are fit with a Lorentzian distribution, where the γ_h is less than half the FWHM.

within reach for Er^{3+}-embedded Si nanophotonic cavities. Homogeneous linewidths that correspond to cooperativity factors above 1 for these Purcell enhancements are therefore promising. Secondly, in addition to the narrow optical homogeneous linewidth, the electron spin coherence time should be sufficiently long to perform several gate operations with low errors. By setting the dephasing rate to approximately once every 1000 gate operations, we set a lower bound on the electron spin coherence time of $T_{2,\mathrm{Hahn}} \geq 1000\tau_\pi$, where τ_π corresponds to the time it takes to perform a π-rotation on the qubit. Third, by observing a second site that fulfils these two optical and spin criteria, we demonstrate that excellent optical and spin properties exist for different Er^{3+} environments in Si rather than being restricted to unusual properties of a unique site. Follow-up measurements can investigate the range over which these sites exist and optimise sample conditions to enhance the prevalence of favourable sites.

In this paper, we use optical detection to investigate both the electron spin and optical transition properties of two Er^{3+} sites within a ^{28}Si (<0.01 % ^{29}Si) crystal. We observe, for the first time in any foundry-compatible semiconductor, long Er^{3+} electron spin coherence times of 0.8 ms and 1.2 ms. In addition, we measure inhomogeneous linewidths of 148 MHz and 72 MHz as well as homogeneous linewidths below 66 kHz and 52 kHz, respectively. Our combined observed optical and spin measurements and the excellent VLSI potential of the silicon host present Er^{3+}:Si as a promising candidate for a broad range of QIP applications.

Results

Photoluminescent excitation spectroscopy

We first characterise Er^{3+} sites in a ^{28}Si sample using photoluminescence excitation (PLE) spectroscopy in a similar approach to ref. 61 using the experimental setup shown in Fig. 1a with no applied radiofrequency (RF) field. The Er^{3+}:Si sample is sandwiched between a fibre ferrule and a superconducting single-photon detector (SSPD). We package two of these sandwiched devices, each containing an Er^{3+}:Si sample from the same wafer, and cool down one device to 20 mK (k_BT/h = 417 MHz) in a dilution refrigerator and the other to 300 mK (k_BT/h = 6.25 GHz) in a ^{3}He system. After calibrating the laser power to ensure consistent optical excitation power across the sampled frequency range, we pulse the laser at a fixed frequency and monitor the laser wavelength using a Bristol 621A wavemeter. The resulting photoluminescence (PL) counts on the SSPD are recorded from 20 μs up to 200 μs after each pulse (Methods). Resonances are observed from 193.4 THz to 197.0 THz for the sample in the dilution refrigerator, as shown in Fig. 1b. The large number of resonances arises from the Er^{3+} ions occupying a combination of substitutional or interstitial Er^{3+}:Si

sites[65,66], with multiple lines resulting from excitation to different crystal field levels (Fig. 1c).

We furthermore observe the same resonances in a sample from the same source, measured in a separate annealing run but under identical annealing conditions. This consistency confirms that site formation is reproducible when using the same sample material and annealing parameters. However, none of the resonances observed in this study overlap with those reported in previous Er:Si studies[61,62,67]. Notably, these earlier studies showed a decrease in the number of resonances with decreasing Er^{3+} concentrations. Following this trend, we expected this sample to exhibit fewer resonances, given that its Er^{3+} concentration is 100 times lower than the Er^{3+} concentration in ref. 61. Nonetheless, we see an approximately equal amount of resonances compared to ref. 61. This result suggests that the different boron background doping in this sample may play a significant role in site formation. Further studies are required to investigate this phenomenon and its underlying mechanisms.

To isolate lines possessing a long electron spin T_1, a prerequisite for a long coherence time, a 10 mT magnetic field is applied along the [110] crystallographic axis (Fig. 1a) to lift the spin degeneracy in each crystal field level (Fig. 1c). For all of the sites we observe here, the ground states form doublets and can be treated as an effective spin-half system with states $|\downarrow\rangle$ and $|\uparrow\rangle$. If T_1 of the spin states is sufficiently long, optically induced spin flips hyperpolarise Er^{3+} ions to non-resonant ground states, e.g., into the $|\uparrow\rangle$ state when exciting transition 1 in Fig. 1c. This reduces the PL signal compared to that observed at zero magnetic field.

The PL intensity can be recovered if a second laser excites the Er^{3+} ions that are shelved into the hyperpolarised state, e.g., transition 2 in Fig. 1c for a hyperpolarised $|\uparrow\rangle$ state. The excitation frequencies under an applied magnetic field (Fig. 1c) can be determined by plotting the PL signal as function of the two laser frequencies, which produces a characteristic pattern shown in Fig. 1d for the 1532.853 nm site (Site E) at B = 10 mT. Here, bright Zeeman resonances appear at laser frequencies of $\pm(f_1 - f_0) = \pm 175$ MHz and $\pm(f_0 + f_1) = \pm 640$ MHz detuned from the centre of the resonance at 0 mT, giving $\Delta f_0/\Delta B = 46.5$ GHz/T ($g = 3.3$) and $\Delta f_1/\Delta B = 81.5$ GHz/T ($g = 5.8$). Sites with symmetry below the T_d symmetry of the crystal will have multiple orientations that may be non-degenerate in the applied field. For Site E, a second orientation with $f_0 = f_1 = 350$ MHz is visible: this orientation gives rise to the bright horizontal and vertical PL lines at zero frequency detuning and the signals near the 3&4 and 4&3 peaks of the first orientation (dotted black circles in Fig. 1d). The different crystal field levels belonging to a single site (Fig. 1b) can be identified by a modification of the above method (Methods). The sites observed in this paper do not contain overlapping resonances with previous Er^{3+}:Si studies[61,62,67]. Besides the different boron background doping, the different sample, implantation and annealing conditions can furthermore contribute to the sites formed and can be investigated in more detail in follow-up studies.

Optical transition measurements

We choose two of the brightest identified sites that exhibit well-distinguished lines under a magnetic field (Site E and Site F) for further investigation (Methods). The inhomogeneous lines of these sites are displayed in Fig. 2a and fit a Lorentzian lineshape, which is consistent with previous studies[61,62,68]. Site E shows consistent full width at half maximum (FWHM) of the inhomogeneous lines of around 150 MHz, whereas the linewidths of the different crystal field transitions of Site F vary, with FWHM values of 145 MHz, 72 MHz and 575 MHz.

We attribute the larger linewidth of the third crystal-field level excitation, compared to the lower crystal-field level excitations, to homogeneous broadening arising from a fast decay from the third, to the first and second crystal-field level in the $^4I_{13/2}$ manifold[69,70]. The inhomogeneous linewidths seen here, below 150 MHz, are comparable to the narrowest linewidths observed in bulk Er^{3+} in insulating systems[71] and are less than half the width of any inhomogeneous lines observed to date for thin-region implanted Er^{3+}:Si[61,62].

We use spectral hole burning on the transition to the lowest $^4I_{13/2}$ crystal field level to investigate the homogeneous linewidths of the two sites. Our method is based on the technique presented in ref. 61, which relies on the saturating behaviour of an atomic transition as a function of the excitation rate R, i.e., $I(2R) < 2I(R)$, where I is the inhomogeneous line intensity. The excitation rate depends on the frequency detuning Δf between two consecutive excitation pulses with equal power P[61], which enables spectral hole burning in the Er^{3+} inhomogeneous line. We significantly increase the signal-to-noise ratio (SNR) of this technique by implementing the following modifications [See Supplemental Materials]: two frequency detuned optical pulses occur simultaneously, and this bichromatic excitation is repeated N_{exp} times every Δf_{comb} over the inhomogeneous peak, resulting in a frequency comb (Fig. 2b). We keep Δf_{comb} much larger than the power broadened homogeneous linewidth at the used optical power. This ensures that probed Er^{3+} subsets within the inhomogeneous line spectrally overlap with a single bichromatic excitation. When the frequency detuning between excitation pulses Δf is zero, the total PL intensity is $N_{exp} \cdot I(2R)$ (dashed red line in Fig. 2b). In the case when Δf exceeds the homogeneous linewidth (γ_h), the total PL intensity is given by $2N_{exp} \cdot I(R)$ (solid red line in Fig. 2b). The SNR ratio in this case is increased as $\sqrt{N_{exp}}$. Because the spectral comb generated is similar for Δf and $-\Delta f$, the spectral hole can be mapped by sweeping $\Delta f > 0$ and mirroring the data along $\Delta f = 0$.

Figure 2c shows the resulting spectral holes for each site for a 50 µs pulse at the lowest optical power set by the measurement SNR ratio, i.e., P = 139 nW and P = 35 nW for Site E and Site F, respectively. Because the measured spectral hole is the convolution of two burnt spectral holes (Fig. 2b), γ_h is equal or less than half the spectral hole FWHM[72] [See Supplemental Materials]. Our technique does not require a correction factor of $N_L/4$, unlike the spectral hole burning method which relies on a polychromatic excitation with N_L lines equidistantly spaced in frequency domain[62] [See Supplemental Materials]. Lorentzian hole fits give homogeneous linewidth upper bounds of 66 kHz and 52 kHz for Site E and Site F, respectively. The observed homogeneous linewidths are close to the system spectral resolution limit of approximately 30 kHz set by the laser intrinsic linewidth (10 kHz) and the Fourier limited broadening of the used optical pulses (20 kHz). Future experiments could hence utilise a more stable laser source to obtain narrower bounds on γ_h. Given that our method eliminates the need for a correction factor, the optical properties of the sites presented in this manuscript are the narrowest Er^{3+}:Si linewidths observed thus far[61,62,68].

The optical lifetimes of site E and site F respectively are 365 µs and 345 µs each [See Supplemental Materials]. This translates to Fourier-transform limited linewidths of 436 Hz and 461 Hz. Assuming a branching ratio of 0.2[64], a Purcell enhancement above 800 is therefore sufficient to reach a cooperativity factor above 1. Purcell factors above 650 are commonly reported for Er^{3+} ions that are evanescently coupled to Si nanophotonic cavities[57,64]. In contrast to evanescent coupling, for Er^{3+}:Si, the Er^{3+} ions reside within the nanophotonic cavity, consequently leading to stronger Purcell enhancements due to direct coupling of the Er^{3+} ions to the cavity modes. In conjunction with the high $Q/V > 10^7(n/\lambda)^3$ nanophotonic cavities that are available[73], Er^{3+}:Si appears particularly promising for reaching cooperativity factors above 1.

Spin transition measurements

The spin transition is studied via optically detected magnetic resonance (ODMR) by hyperpolarizing the spin states into the $|\downarrow\rangle$ state, applying an RF pulse to partially repopulate the $|\uparrow\rangle$ state, and using state-selective optical excitation of the $|\uparrow\rangle$ state (transition 2 in Fig. 1c) to measure the Er^{3+} population in the $|\uparrow\rangle$ state. The static magnetic fields of 12.37 mT for Site E and 10.56 mT for Site F, are chosen to match the Zeeman splitting of the site (46.5 GHz/T for Site E, and 64.7 GHz/T for Site F) to the RF antenna resonance frequency: 575 MHz for Site E (^{3}He system), and 683 MHz for Site F (dilution refrigerator).

The ODMR pulse sequence follows either a single RF pulse or a sequence of RF pulses to manipulate the electron spin states. Afterwards, a delay of a few microseconds was implemented to reduce the effect of

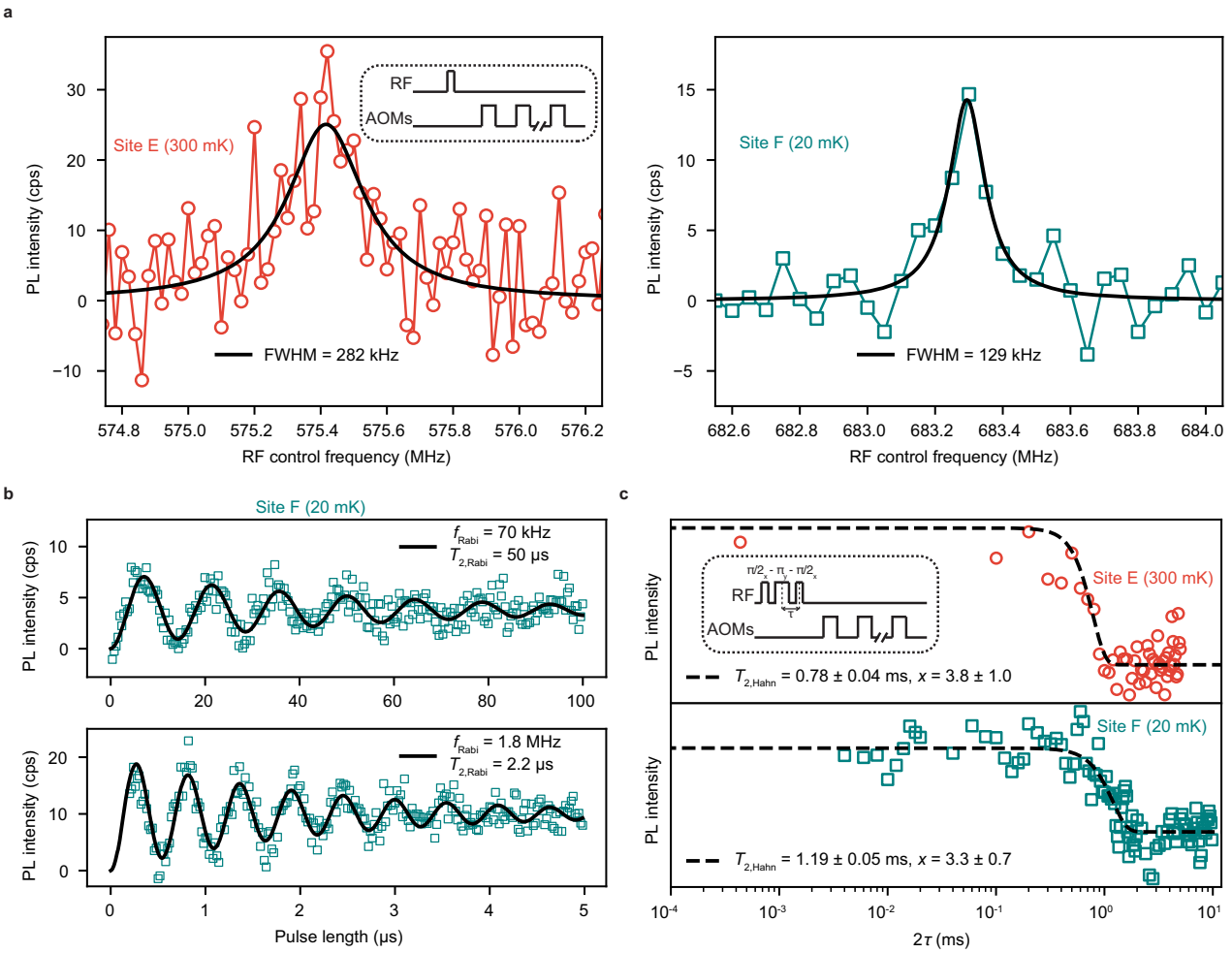

Fig. 3 | Spin transition properties of Site E and Site F. a Optically detected magnetic resonance (ODMR) signal of the spin transition as function of the RF frequency of the antenna at − 10 dBm RF power to the antenna. The static magnetic fields applied are 12.37 mT and 10.56 mT for Site E and Site F, respectively. Both data are fit with a Lorentzian distribution. **a**, inset, The pulse sequence used for obtaining the ODMR signal. **b** ODMR signal of Site F at different radiofrequency (RF) pulse lengths, using the same sequence as in (**a**, inset). **c** Hahn echo decay traces as function of delay between the pulses (τ). Both Site E and Site F show long electron spin coherence time at 300 mK and 20 mK, respectively. **c**, inset, The Hahn echo pulse sequence used. Here, a final $\frac{\pi}{2_x}$ ($\frac{-\pi}{2_x}$) is applied to project the spin states to the $|\uparrow\rangle$ ($|\downarrow\rangle$) state. This allows optical state-selective excitation to extract the ODMR signal. The duration of each of these measurements is approximately two hours.

heating on the count rate by bringing the SSPD back to the superconducting state before the optical readout pulses. We then repeat a series of optical pulses with a pulse length of t_{pulse} followed by a readout time of length $t_{collection}$ for reading out the spin states, which simultaneously reinitializes the spin states. The pulse length and collection time are optimized to maximize the SNR during the collection sequence, leading to microsecond pulse lengths and collection times slightly shorter than the optical lifetime. We furthermore perform cyclicity measurements using these parameters to ensure the spin states are fully reinitialized before the following RF sequence [Methods].

In these measurements, the spin splitting of site F (k_BT/h = 683 MHz) is more than the thermal energy corresponding to the dilution refrigerator (k_BT/h = 417 MHz) and the spin splitting of site E (k_BT/h = 575 MHz) is less than the thermal energy of the ^{3}He system (k_BT/h = 6.25 GHz) they were measured in, respectively. Due to the application of optical and microwave pulses, the sample temperature in the dilution refrigerator is expected to be higher than the mixing chamber temperature, resulting in a thermal energy that is comparable to or greater than the energy difference between the spin states. This makes accurately determining the spin temperature challenging. We therefore expect that the spin-up and spin-down states within each sample have nearly equal populations at thermal equilibrium.

Decreasing the RF power in the ODMR measurements results in narrower spin inhomogeneous linewidths, indicating power broadening at higher RF powers [See Supplemental Materials]. For Site E, a FWHM of 282 kHz is observed at − 10 dBm RF power to the antenna (Fig. 3a). This site shows a long term drift of ± 0.5 MHz over minutes. The drift to higher frequencies likely indicates the sample holder moving in the field of the (persistent-mode) superconducting magnet in the ^{3}He system. The corresponding linewidth of Site F at an equivalent − 10 dBm of RF power is 129 kHz (Fig. 3a), with no observable long term drift, attributed to a more stable setup in the dilution refrigerator, allowing the observation of a narrower linewidth.

Rabi oscillations are obtained by varying the RF pulse length with the frequency tuned to the centre of the inhomogeneous spin line. Here, we focus on Site F due to the better long term stability of that setup. The Rabi oscillations are fit with

$$P_{0\to1} = A[1 - \exp(-t/T_{2,\mathrm{Rabi}})]\cos(2\pi f_{\mathrm{Rabi}} t), \quad (1)$$

where A is the amplitude, t is the pulse length, $T_{2,\mathrm{Rabi}}$ is the Rabi decay constant and f_{Rabi} is the Rabi frequency. For − 16 dBm RF power to the antenna, f_{Rabi} = 70 kHz and $T_{2,\mathrm{Rabi}}$ = 50 μs, while at 12 dBm power, f_{Rabi} increases to 1.8 MHz and $T_{2,\mathrm{Rabi}}$ decreases to 2.2 μs (Fig. 3b). Pulse widths

shorter than 350 ns are not applied due to limitations on the RF source, as well as the 15 MHz bandwidth of the RF antenna. The experiments are furthermore constrained to the RF powers from − 16 dBm to 12 dBm because the ODMR signal diminishes at lower RF powers, while higher powers introduce heating effects, evidenced by increased SSPD count rates and elevated cryostat temperature readings. These measurements are repeated on Site E at 300 mK, where we similarly extract a Rabi frequency up to 1.7 MHz [See Supplemental Materials].

The high Rabi frequency seen here is comparable with other state-of-the-art electron spin qubit systems in silicon[13–15,23], and indicates fast spin-flip operations are possible for Er^{3+} ions in silicon. The Rabi frequencies scale linearly with the applied electric field, i.e. $f_{\mathrm{Rabi}} \propto \sqrt{P}$, rather than showing a saturation of the Rabi frequencies at these powers [See Supplemental Materials], which has been observed in semiconductor spin qubits at high RF powers[22,74–78]. Hence, higher Rabi frequencies are expected to be observable by optimising the antenna geometry to allow higher magnetic fields with less heat dissipation.

A Hahn echo sequence[79] is used to measure the decoherence time ($T_{2,\mathrm{Hahn}}$) of Site E and Site F. To optically detect the resulting refocused Er^{3+} spins, we apply an additional $\frac{\pi}{2_x}$ (or $-\frac{\pi}{2_x}$) pulse after the refocusing to project the spin states in the $|\uparrow\rangle$ ($|\downarrow\rangle$) state and then use state-selective excitation to probe the spin state population (Fig. 1c). We record the signal for varying time τ for two sequences (final $\frac{\pi}{2_x}$ or final $-\frac{\pi}{2_x}$) and subtract the two signals to remove background counts, giving a signal decay depending only on $T_{2,\mathrm{Hahn}}$ (Fig. 3c). This trace is fit with:

$$I = A\exp[-(\tau/T_{2,\mathrm{Hahn}})^x], \quad (2)$$

where A is the fluorescence amplitude, $T_{2,\mathrm{Hahn}}$ is the exponential decay constant and x is the stretch factor that can indicate the dominant decoherence mechanism[63].

The Hahn traces for Site E and Site F exhibit a sharp decay around 1 ms that is best fit to a stretched exponential with stretch factors of 3.8 ± 1.1 and 3.3 ± 0.7, respectively. This remarkable 100-fold improvement in the Hahn echo time for Er^{3+} sites in Si, compared to the previously reported coherence time of 7.5 µs measured for a different Er^{3+} site at a higher temperature, can be attributed, as suggested in ref. 63, to superhyperfine coupling with ^{29}Si spins. The hypothesis that ^{29}Si spins are the primary factor limiting spin coherence time in natural Si samples is further corroborated by our measurement of the coherence time for site F in a natural silicon sample [see Supplemental Materials].

Stretch factors greater than one have also been reported in P:^{28}Si qubits in cryogenic systems[80,81], where spin coherence times are similarly limited to around one millisecond. In ref. 80, these larger stretch factors were attributed to external influences, such as superconducting magnetic noise, likely caused by mechanical vibrations or flux creep. Similarly, ref. 81 observed stretch factors ranging from 2 to 3, attributing them to a phase mismatch between the instrument and the in-phase Larmor frequencies.

The similarities between our findings and setup, such as the potential for inducing acoustic vibrations via pulse tubes or roughing pumps, suggest that the observed stretch factors and millisecond-scale coherence times in our study are also predominantly limited by external sources. To better understand the intrinsic factors limiting electron spin coherence times, such as residual ^{29}Si spin noise or site symmetries, future studies on Er^{3+} systems should focus on establishing a higher bound for $T_{2,\mathrm{Hahn}}$. Achieving this will require addressing acoustic vibrations, mitigating instrumental phase noise, and, in the context of ESR measurements, taking the amplitude of the ESR signal[81].

These measurements therefore introduce a lower limit on $T_{2,\mathrm{Hahn}}$ of 0.78 ± 0.04 ms and 1.19 ± 0.05 ms for Site E and Site F, as extracted from the fits to the stretched exponential. As presented before, both sites exhibit Rabi frequencies exceeding 1.7 MHz. These observed Rabi frequencies require a minimum $T_{2,\mathrm{Hahn}}$ time of 294 µs to ensure, on average, that a phase flip occurs once every 1000 π-rotation operations. Furthermore, we expect that these coherence times will also set the lower bound for single Er^{3+} ions at these depths, as these ions will be subjected to a lower magnetic noise due to the lower Er^{3+} concentration. In addition, we observe spin-lattice relaxation times of 10.9 s and 23.8 s respectively for site E and F under 20 mK and 10.56 mT [See Supplemental Material]. Since the observed Hahn echo times surpass the required $T_{2,\mathrm{Hahn}}$ threshold, the electron spin properties, along with the optical transition properties, position Er^{3+}:Si sites as promising candidates for QIP applications.

Discussion

In this study, we investigated Er^{3+} ions in ^{28}Si at two sites and observed narrow optical linewidths and millisecond ground electron spin coherence times in both sites. These long coherence times indicated that Er^{3+}:Si meets the fundamental requirements of a versatile telecom-compatible spin-photon interface in silicon. The findings of this study, which focuses on measurements conducted on Er^{3+} ions implanted at a depth ranging from 200 nm to 700 nm, are particularly relevant to employing Er^{3+}-implanted micrometre-thick ultra-low-loss silicon on-insulator (SOI) devices for QIP applications[82,83]. Furthermore, L3 photonic crystal cavities with high Q/V ratios can be realised in multimode membranes as confirmed by comparable Purcell factors achieved in GaAs photonic crystal cavities fabricated in multimode[84] and single mode[85] membranes. Here, the VLSI potential of silicon can be harnessed to fabricate photonic devices such as Er^{3+}:Si implanted SOI nanophotonic cavities in order to enhance the emission rate or achieve non-linear effects[48,49,86]. Future Er^{3+}:Si research can also benefit from the increasingly accessibility of ^{28}Si or ^{28}Si-on-insulator wafers, which are realised through new approaches such as high fluence ^{28}Si ion implantation[87] or molecular-beam epitaxy growth[88].

We showed that the optical homogeneous linewidth of both sites is less than 70 kHz. This itself is already narrow, confirming these sites as good optical quantum information candidates, but the prospect of a much narrower true linewidth motivates additional study to extract the true linewidth. Photon echo methods, while challenging for such small ensembles, can provide the required accuracy at the same time as allowing another important parameter, the spectral diffusion, to be measured. The current measurements can only limit the spectral diffusion on timescales less than the pulse length (50 µs) to be less than 70 kHz. QIP applications for Er^{3+}:Si, such as sources of indistinguishable photons, typically require medium or long-term stability in the optical frequency and, therefore, low spectral diffusion. This is a challenge for many optical centres, particularly in nanophotonic structures where surface states and other fabrication effects lead to both line broadening and spectral diffusion on short and long timescales[89,90]. Fortunately, Er^{3+} lines tend to remain narrow and stable because their low electric field susceptibility generates a weak sensitivity to noise and defects[57,62].

Optical linewidths of comparable magnitude have been observed for Er^{3+} ions in insulators and $CaWO_4$[57,64,91], where narrow optical linewidths have been associated with non-polar site symmetries. The similar linewidths of the two sites presented in this manuscript could therefore suggest that these sites likewise exhibit non-polar group symmetries. The non-polar symmetry will contribute to preserve good optical coherence properties when the Er^{3+} ions are situated nearer to the surface in photonic structures. Literature furthermore reveals that optically active Er^{3+}-only sites have been identified in samples with low oxygen concentration[62,67]. Given that the O concentration in this study is hundredfold lower than that of Er^{3+} to mitigate the creation of Er–O clusters, we anticipate that these sites are potentially optically active Er^{3+}-only complexes[66,92,93]. Additional investigations are necessary to thoroughly examine the structural properties of these sites.

The current sample can readily be utilised for ensemble-based QIP protocols, however, for protocols based on single Er^{3+} ions, methods such as large-scale characterisation with post-selective nanofabrication[94] or localised optical excitation through free-space optics for cluster state generation[95] can be utilised to address single Er^{3+} ions residing within a site with good quantum properties. In addition, the yield of Er^{3+} ions residing within a particular site can be further improved through varying implantation and annealing conditions[62,67].

These Er^{3+} sites can be compared to the other optical spin photon candidate in a telecom band, the silicon T centre, a complex carbon-related radiation defect with a 1326 nm transition in the O-band[23,46]. In ^{28}Si, both sites have comparable electron spin coherence times of 2.1 ms (T centre) and 1.2 ms (Er^{3+}), and optical inhomogeneous linewidths of 33 MHz[23] (T centre) and 72 MHz (Er^{3+}). Their other optical properties place them in different, complementary regimes: the T centre has a stronger oscillator strength of 10^{-4} and an associated µs short lifetime[23,96], and broad homogeneous line of 690 kHz[97] with 27 MHz of spectral diffusion[90], while Er^{3+} has a weaker oscillator strength (not measured in silicon, but 10^{-7} is typical[70]), 0.1 ms to 1.6 ms lifetimes[61,62] and very narrow homogeneous lines below 70 kHz. Both optical centres are in similar, initial stages of study, but already show significant appeal for spin-photon interfaces. Further development is likely to improve key properties and elucidate the regimes and applications best suited to each centre.

This work shows for the first time that Er^{3+}:Si meets the spin and optical coherence time requirements for a spin-photon interface. Taken together with the unmatched mature fabrication technology existing in silicon, these properties present Er^{3+}:Si as a promising material of high interest for realising a scalable, telecommunication-compatible platform for quantum computing and quantum network applications.

Methods

Implant and anneal recipe

The two ^{28}Si samples both originate from the material used for the study in ref. 98, which contains a background doping of B at approximately 1×10^{15} cm^{-3}. To study the optical transitions without the complication of hyperfine structure, the nuclear-spin-free ^{170}Er isotope is implanted with ion energies of 800, 1200 and 2000 keV and, respectively, ion fluences of 9×10^{10}, 1.4×10^{11} and 3.1×10^{11} cm^{-2} into one side of the 490 µm double-side-polished ^{28}Si wafer to form a uniform concentration profile of 1×10^{16} cm^{-3} over a depth of 200 nm to 700 nm. Following implantation, the wafers are consecutively diced and annealed at 700 °C for 10 min in an N_2 atmosphere, which is known to lead to optically active Er^{3+} ions in silicon[61,62,68,99].

Photoluminescent excitation spectroscopy

The emission of the Er^{3+} ions is collected by an in-situ SSPD as presented in ref. 61. Here, a ferrule containing a CCC1310-J9 fibre was polished and used to sandwich the sample between the SSPD and the ferrule. To obtain the PLE spectrum, the laser frequency is swept from 190.70 THz to 197.36 THz (1572 nm to 1519 nm) in steps of 20 MHz.

In addition to this in-situ detection configuration, we add a single-layer coiled copper wire antenna between the sample and the fibre ferrule for the RF control of the electron spins. The inner diameter of the copper coil is larger than the mode diameter of the laser light emitted from the fibre end, thus providing an unobstructed path for the laser light to reach the sample. This copper wire is present, but unused during the PLE scan.

One ^{28}Si sample is situated in a dilution refrigerator at a temperature of 20 mK, and one ^{28}Si sample in a ^3He system at a temperature of 300 mK. These low temperatures are to ensure a low dark count rate on the SSPD, and long spin-lattice and spin-spin relaxation times. Moreover, these temperatures are low enough to minimise non-radiative recombination of the Er^{3+} optical transition[100–102].

To excite the Er^{3+} ions, we use a semiconductor diode laser (Pure Photonics PPCL550) with an output pulse modulated by two acousto-optical modulators (AOMs) connected in series, resulting in an extinction ratio greater than 100 dB, similar to the excitation schematic in ref. 61. After the excitation pulse, we record the number of counts from the SSPD for 200 µs with a digital counter (Keysight 53131A or National Instruments PCI-6602). The SSPD current bias is set to zero during the excitation pulse and is reset to its nominal value 20 µs after the excitation pulse. This SSPD blanking mitigates the current-induced Joule heating, hence allowing a faster reset time after the excitation pulse is extinguished[61]. For this reason, the counts in the first 20 µs after the excitation pulse are ignored in all PLE measurements.

PLE spectrum site extraction

The resonances in the PLE spectrum belonging to the same site can be identified with a modification of the two-colour excitation sequence used to recover the Zeeman spectrum: instead of shifting the frequency of the second laser by a small amount to excite one of the transitions to the same excited state Zeeman doublet, it is shifted to the centre of a different line in the PLE spectrum. If this causes the recovery of the signal, that line is a higher energy crystal field line belonging to the same site [See Supplemental Materials], and by testing all lines in the spectrum, all visible transitions associated with one site can be determined. This procedure is performed on the 7 brightest resonances exhibiting long-lived spin states, identifying them as arising from seven sites with long electron spin lifetimes (Fig. 1b and Supplementary Table 1 Resonances with long-lived electron spin states). Of these sites, Site F exhibits the brightest resonance within the PLE spectrum at 195571 GHz, and is therefore the first resonance we used for spin coherence time measurements. We furthermore choose Site E as a second resonance to measure to confirm that the characteristics of Site F were not solely limited to one site. Site E is the third-brightest and produced the clear Zeeman pattern shown in Fig. 1d; Site C, the second brightest, is excluded due to its unclear Zeeman pattern indicating a large number of site orientations, which results in a lower intensity per Zeeman transition.

Optically detected magnetic resonance spectroscopy

To control the electron spin states, we use RF pulses from the copper coil generated by a Keysight N5182B vector source. In order to mitigate the heat load of the RF antenna, we introduce an *LC* circuit to enhance the RF emission at a desired resonance frequency. We set the resonance frequency at approximately 600 MHz, which is high enough to distinguish the two $\Delta M_S = 0$ optical transitions as seen in Fig. 1d, hence allowing state-selective optical excitation.

The *LC* circuit is formed by adding two capacitors to the copper wire antenna: one capacitor is connected in series to set the resonance frequency of the antenna, and the other capacitor is connected in parallel to match the impedance. The resulting resonance frequency is measured by sweeping the reflection of the antenna as function of the RF frequency using a 9 GHz Keysight FieldFox. The resonance frequency of the antenna in the dilution refrigerator is 683 MHz at a bandwidth of 15 MHz, and the resonance frequency of the antenna in the ^3He system is 590 MHz with a bandwidth of 20 MHz.

Cyclicity measurements

We measure the number of optical pulses required to depolarise a spin state, depending on the cyclicity of the optical transition excited. During the ODMR sequence, a number of optical pulses are applied after the RF pulse for two reasons: to initialise the spin state and to enhance the SNR of the collected PL. The number of optical pulses after the RF sequence is chosen such that $N_{\text{pulses}} > N_{\text{cyclicity}}$, where N_{pulses} is the number of pulses after the RF sequence and $N_{\text{cyclicity}}$ the number of optical pulses needed to depolarise the spin states, depending on the optical pulse length and power specific to the measurements. After every optical pulse in this state-selective optical sequence, the PL is collected. For our measurement, we excite the $\Delta M_S = 0$ transitions [red solid lines in Fig. 1c].

To measure the cyclicity, an electro-optical modulator (EOM) was used to rapidly change the excitation frequency. A frequency of 3 GHz was applied on the EOM, leading to a single carrier and two sidebands. The carrier was suppressed by changing the polarisation of the light and by optimising the DC voltage to the EOM. One of the remaining two sidebands was centred on the resonance belonging to the $|\downarrow\rangle$ transition for the pump pulse and the other sideband was located off-resonantly 3 GHz at a lower frequency. The $|\downarrow\rangle$ transition is depolarised by exciting this transition for 1 ms at 120 µW (60 µW per sideband) of optical power on the sample. Afterwards, the frequency of the sideband is set to the transition in resonance with the $|\uparrow\rangle$ transition to initiate the probe sequence. The probe sequence consists of a number of excitation pulses of 10 µs at the same optical power on the sample, which are spaced 200 µs apart. The PL is

collected in the 200 μs bins, of which we ignore the first 20 μs due to the SSPD recovery time as explained in Methods. This sequence is repeated 200 times and the PL at each pulse number is averaged. This sequence was repeated with the pump pulse off-resonantly centred 200 MHz from the $|\downarrow\rangle$ transition [See Supplemental Materials for the cyclicity measurement on Site E].

As expected, the count rate of the on-resonant curve is higher than the off-resonant curve due to PL excitation of the hyperpolarised $|\downarrow\rangle$ state, and eventually reaches the same PL intensity after the $|\downarrow\rangle$ state is depolarised. During the ODMR measurements, the same optical parameters of 10 μs pulse length and 60 μW of optical power were used to depolarise and read out the spin states.

Notes

During the review of this manuscript, the authors became aware of a manuscript reporting on ODMR measurements of single Er^{3+} ions in ^{nat}Si photonic cavities[103].

Data availability

The data that support the plots within this paper and other findings of this study are available from the corresponding author upon request.

Code availability

The computer codes that support the plots within this paper and other findings of this study are available from the corresponding author upon request.

Received: 5 August 2024; Accepted: 11 March 2025;
Published online: 18 April 2025

References

1. Nielsen, M. A. & Chuang, I. L. *Quantum computation and quantum information*, https://www.google.com.au/books/edition/Quantum_Computation_and_Quantum_Informat/-s4DEy7o-a0C?hl=en&gbpv=0 (Cambridge University Press, 2010), 10th anniversary edn.
2. Shor, P. W. Polynomial-time algorithms for prime factorization and discrete logarithms on a quantum computer. *Siam J. Comput.* **26**, 1484–1509 (1997).
3. Grover, L. K. A fast quantum mechanical algorithm for database search https://doi.org/10.1145/237814.237866 (1996).
4. Wehner, S., Elkouss, D. & Hanson, R. Quantum internet: A vision for the road ahead. *Science* **362**, eaam9288 (2018).
5. Childs, A. M. & van Dam, W. Quantum algorithms for algebraic problems. *Rev. Mod. Phys.* **82**, 1–52 (2010).
6. Divincenzo, D. P. Quantum computation. *Science* **270**, 255–261 (1995).
7. Ekert, A. & Jozsa, R. Quantum computation and shor's factoring algorithm. *Rev. Mod. Phys.* **68**, 733–753 (1996).
8. Feynman, R. P. Simulating physics with computers. *Int. J. Theor. Phys.* **21**, 467–488 (1982).
9. Jordan, S. Quantum algorithm zoo https://quantumalgorithmzoo.org (2011).
10. Montanaro, A. Quantum algorithms: an overview. *Npj Quantum Inf.* **2**, 15023 (2016).
11. Alexeev, Y. et al. Quantum computer systems for scientific discovery. *PRX Quantum* **2**, 017001 (2021).
12. Kane, B. E. A silicon-based nuclear spin quantum computer. *Nature* **393**, 133–137 (1998).
13. Pla, J. J. et al. A single-atom electron spin qubit in silicon. *Nature* **489**, 541–545 (2012).
14. Fricke, L. et al. Coherent control of a donor-molecule electron spin qubit in silicon. *Nat. Commun.* **12**, 3323 (2021).
15. Philips, S. G. J. et al. Universal control of a six-qubit quantum processor in silicon. *Nature* **609**, 919–924 (2022).
16. Burkard, G., Ladd, T. D., Nichol, J. M., Pan, A. & Petta, J. R. Semiconductor spin qubits https://ui.adsabs.harvard.edu/abs/2021arXiv211208863B (2021).
17. Tyryshkin, A. M. et al. Electron spin coherence exceeding seconds in high-purity silicon. *Nat. Mater.* **11**, 143–147 (2012).
18. Veldhorst, M. et al. An addressable quantum dot qubit with fault-tolerant control-fidelity. *Nat. Nanotechnol.* **9**, 981–985 (2014).
19. Takeda, K., Noiri, A., Nakajima, T., Kobayashi, T. & Tarucha, S. Quantum error correction with silicon spin qubits. *Nature* **608**, 682–686 (2022).
20. Veldhorst, M. et al. A two-qubit logic gate in silicon. *Nature* **526**, 410–414 (2015).
21. Xue, X. et al. Quantum logic with spin qubits crossing the surface code threshold. *Nature* **601**, 343–347 (2022).
22. Yoneda, J. et al. A quantum-dot spin qubit with coherence limited by charge noise and fidelity higher than 99.9%. *Nat. Nanotechnol.* **13**, 102–106 (2018).
23. Bergeron, L. et al. Silicon-integrated telecommunications photon-spin interface. *PRX Quantum* **1**, 020301 (2020).
24. El-Kareh, B. *Fundamentals of semiconductor processing technologies*. (Kluwer Academic Publishers, Boston, 1995).
25. Li, R. et al. A crossbar network for silicon quantum dot qubits. *Sci. Adv.* **4**, eaar3960 (2018).
26. Jones, C. et al. Logical qubit in a linear array of semiconductor quantum dots. *Phys. Rev. X* **8**, 021058 (2018).
27. Zajac, D. M., Hazard, T. M., Mi, X., Nielsen, E. & Petta, J. R. Scalable gate architecture for a one-dimensional array of semiconductor spin qubits. *Phys. Rev. Appl.* **6**, 054013 (2016).
28. Zwerver, A. M. J. et al. Qubits made by advanced semiconductor manufacturing. *Nat. Electron.* **5**, 184–190 (2022).
29. Vandersypen, L. M. K. et al. Interfacing spin qubits in quantum dots and donors-hot, dense, and coherent. *npj Quantum Inf.* **3**, 34 (2017).
30. Borjans, F., Croot, X. G., Mi, X., Gullans, M. J. & Petta, J. R. Resonant microwave-mediated interactions between distant electron spins. *Nature* **577**, 195–198 (2020).
31. Yan, X. R. et al. Silicon photonic quantum computing with spin qubits. *APL Photonics* **6**, 070901 (2021).
32. Harvey-Collard, P. et al. Coherent spin-spin coupling mediated by virtual microwave photons. *Phys. Rev. X* **12**, 021026 (2022).
33. Kimble, H. J. The quantum internet. *Nature* **453**, 1023–1030 (2008).
34. Borregaard, J., Sorensen, A. S. & Lodahl, P. Quantum networks with deterministic spin-photon interfaces. *Adv. Quantum Technol.* **2**, 1800091 (2019).
35. Zhu, X. Y. et al. Spin-photon module for scalable network architecture in quantum dots. *Sci. Rep.* **10**, 5063 (2020).
36. Singal, T. *Optical Fiber Communications: Principles and Applications* https://books.google.com.au/books?id=_JheDwAAQBAJ (Cambridge University Press, 2017).
37. Panuski, C., Englund, D. & Hamerly, R. Fundamental thermal noise limits for optical microcavities. *Phys. Rev. X* **10**, 041046 (2020).
38. Liu, J. Q. et al. High-yield, wafer-scale fabrication of ultralow-loss, dispersion-engineered silicon nitride photonic circuits. *Nat. Commun.* **12**, 2236 (2021).
39. Edinger, P. et al. Silicon photonic microelectromechanical phase shifters for scalable programmable photonics. *Opt. Lett.* **46**, 5671–5674 (2021).
40. Gyger, S. et al. Reconfigurable photonics with on-chip single-photon detectors. *Nat. Commun.* **12**, 1408 (2021).
41. Chakraborty, U. et al. Cryogenic operation of silicon photonic modulators based on the dc kerr effect. *Optica* **7**, 1385–1390 (2020).
42. Redjem, W. et al. Single artificial atoms in silicon emitting at telecom wavelengths. *Nat. Electron.* **3**, 738–743 (2020).
43. Prabhu, M. et al. Individually addressable and spectrally programmable artificial atoms in silicon photonics. *Nat. Commun.* **14**, 2380 (2023).

44. Redjem, W. et al. All-silicon quantum light source by embedding an atomic emissive center in a nanophotonic cavity. *Nat. Commun.* **14**, 3321 (2023).
45. Hollenbach, M. et al. Wafer-scale nanofabrication of telecom single-photon emitters in silicon. *Nat. Commun.* **13**, 7683 (2022).
46. Higginbottom, D. B. et al. Optical observation of single spins in silicon. *Nature* **607**, 266–270 (2022).
47. Higginbottom, D. B. et al. Memory and transduction prospects for silicon t center devices. *PRX Quantum* **4**, 020308 (2023).
48. Duan, L. M. & Kimble, H. J. Scalable photonic quantum computation through cavity-assisted interactions. *Phys. Rev. Lett.* **92**, 127902 (2004).
49. McAuslan, D. L., Longdell, J. J. & Sellars, M. J. Strong-coupling cavity qed using rare-earth-metal-ion dopants in monolithic resonators: What you can do with a weak oscillator. *Phys. Rev. A* **80**, 062307 (2009).
50. Böttger, T., Thiel, C. W., Cone, R. L. & Sun, Y. Effects of magnetic field orientation on optical decoherence in er^{3+}: y_2sio_5. *Phys. Rev. B* **79**, 115104 (2009).
51. Rančić, M., Hedges, M. P., Ahlefeldt, R. L. & Sellars, M. J. Coherence time of over a second in a telecom-compatible quantum memory storage material. *Nat. Phys.* **14**, 50–54 (2018).
52. Le Dantec, M. et al. Twenty-three-millisecond electron spin coherence of erbium ions in a natural-abundance crystal. *Sci. Adv.* **7**, eabj9786 (2021).
53. Williamson, L. A., Chen, Y. H. & Longdell, J. J. Magneto-optic modulator with unit quantum efficiency. *Phys. Rev. Lett.* **113**, 203601 (2014).
54. Fernandez-Gonzalvo, X., Chen, Y. H., Yin, C. M., Rogge, S. & Longdell, J. J. Coherent frequency up-conversion of microwaves to the optical telecommunications band in an er:yso crystal. *Phys. Rev. A* **92**, 062313 (2015).
55. Fernandez-Gonzalvo, X., Horvath, S. P., Chen, Y. H. & Longdell, J. J. Cavity-enhanced raman heterodyne spectroscopy in er3+:y2sio5 for microwave to optical signal conversion. *Phys. Rev. A* **100**, 033807 (2019).
56. Rochman, J., Xie, T., Bartholomew, J. G., Schwab, K. C. & Faraon, A. Microwave-to-optical transduction with erbium ions coupled to planar photonic and superconducting resonators. *Nat. Commun.* **14**, 1153 (2023).
57. Ourari, S. et al. Indistinguishable telecom band photons from a single erbium ion in the solid state. *arXiv*, https://arxiv.org/abs/2301.03564 (2023).
58. Raha, M. et al. Optical quantum nondemolition measurement of a single rare earth ion qubit. *Nat. Commun.* **11**, 1605 (2020).
59. Yang, L. K., Wang, S. H., Shen, M. H., Xie, J. C. & Tang, H. X. Controlling single rare earth ion emission in an electro-optical nanocavity. *Nat. Commun.* **14**, 1718 (2023).
60. Wang, Z. et al. Single-electron spin resonance detection by microwave photon counting. *Nature* **619**, 276–281 (2023).
61. Berkman, I. R. et al. Observing er^{3+} sites in si with an in situ single-photon detector. *Phys. Rev. Appl.* **19**, 014037 (2023).
62. Gritsch, A., Weiss, L., Fruh, J., Rinner, S. & Reiserer, A. Narrow optical transitions in erbium-implanted silicon waveguides. *Phys. Rev. X* **12**, 041009 (2022).
63. Hughes, M. A. et al. Spin echo from erbium implanted silicon. *Appl. Phys. Lett.* **118**, 194001 (2021).
64. Dibos, A., Raha, M., Phenicie, C. & Thompson, J. D. Atomic source of single photons in the telecom band. *Phys. Rev. Lett.* **120**, 243601 (2018).
65. Kenyon, A. J. Erbium in silicon. *Semiconductor Sci. Technol.* **20**, R65–R84 (2005).
66. Przybylińska, H. et al. Optically active erbium centers in silicon. *Phys. Rev. B* **54**, 2532–2547 (1996).
67. Rinner, S., Burger, F., Gritsch, A., Schmitt, J. & Reiserer, A. Erbium emitters in commercially fabricated nanophotonic silicon waveguides. *Nanophotonics* **12**, 3455–3462 (2023).
68. Weiss, L., Gritsch, A., Merkel, B. & Reiserer, A. Erbium dopants in nanophotonic silicon waveguides. *Optica* **8**, 40–41 (2021).
69. Lauritzen, B., Hastings-Simon, S. R., de Riedmatten, H., Afzelius, M. & Gisin, N. State preparation by optical pumping in erbium-doped solids using stimulated emission and spin mixing. *Phys. Rev. A* **78**, 043402 (2008).
70. Sun, Y. C. Rare earth materials in optical storage and data processing applications. In: *Spectroscopic Properties of Rare Earths in Optical Materials*, Springer series in materials science, 412 (eds, Liu, G. & Jacquier, B.) https://doi.org/10.1007/3-540-28209-2 (Springer Berlin, Heidelberg, Berlin, 2005).
71. Macfarlane, R. M., Cassanho, A. & Meltzer, R. S. Inhomogeneous broadening by nuclear-spin fields - a new limit for optical-transitions in solids. *Phys. Rev. Lett.* **69**, 542–545 (1992).
72. Bjorklund, G. C. In Moerner, W. E. (ed.) *Persistent Spectral Hole-Burning: Science and Applications*, **1**, 5 (Springer-Verlag Berlin Heidelberg, 1988).
73. Panuski, C. L. et al. A full degree-of-freedom spatiotemporal light modulator. *Nat. Photonics* **16**, 834–842 (2022).
74. Vahapoglu, E. et al. Coherent control of electron spin qubits in silicon using a global field. *npj Quantum Inf.* **8**, 126 (2022).
75. Undseth, B. et al. Nonlinear response and crosstalk of electrically driven silicon spin qubits. *Phys. Rev. Appl.* **19**, 044078 (2023).
76. Yoneda, J. et al. Fast electrical control of single electron spins in quantum dots with vanishing influence from nuclear spins. *Phys. Rev. Lett.* **113**, 267601 (2014).
77. Takeda, K. et al. A fault-tolerant addressable spin qubit in a natural silicon quantum dot. *Sci. Adv.* **2**, e1600694 (2016).
78. Nakajima, T. et al. Coherence of a driven electron spin qubit actively decoupled from quasistatic noise. *Phys. Rev. X* **10**, 011060 (2020).
79. Hahn, E. L. Spin echoes. *Phys. Rev.* **80**, 580–594 (1950).
80. Storing quantum information for 30 seconds in a nanoelectronic device. *Nature Nanotechnol.* **9**, 986–991 (2014).
81. Tyryshkin, A. M. et al. Coherence of spin qubits in silicon. *J. Phys.-Condens. Matter* **18**, S783–S794 (2006).
82. Cherchi, M. et al. Supporting quantum technologies with an ultralow-loss silicon photonics platform. *Adv. Photonics Nexus* **2**, 024002–024002 (2023).
83. Marin, Y. E., Bera, A., Cherchi, M. & Aalto, T. Ultra-high-q racetrack resonators on thick soi platform through hydrogen annealing smoothing. *J. Lightwave Technol.* **41**, 3642–3648 (2023).
84. Huang, J. et al. Exciton-polariton dynamics of the single site-controlled quantum dot-nanocavity in the coexisting strong-weak coupling regime. *N. J. Phys.* **25**, 033015 (2023).
85. Hennessy, K. et al. Quantum nature of a strongly coupled single quantum dot–cavity system. *Nature* **445**, 896–899 (2007).
86. Gritsch, A., Ulanowski, A. & Reiserer, A. Purcell enhancement of single-photon emitters in silicon. *Optica* **10**, 783–789 (2023).
87. Holmes, D. et al. Isotopic enrichment of silicon by high fluence si-28(-) ion implantation. *Phys. Rev. Mater.* **5**, 014601 (2021).
88. Liu, Y. et al. 28silicon-on-insulator for optically interfaced quantum emitters. *J. Cryst. Growth* **593**, 126733 (2022).
89. Sangtawesin, S. et al. Origins of diamond surface noise probed by correlating single-spin measurements with surface spectroscopy. *Phys. Rev. X* **9**, 031052 (2019).
90. MacQuarrie, E. R. et al. Generating t centres in photonic silicon-on-insulator material by ion implantation. *N. J. Phys.* **23**, 103008 (2021).
91. Gupta, S. et al. Dual epitaxial telecom spin-photon interfaces with correlated long-lived coherence. *arXiv*, https://arxiv.org/abs/2310.07120 (2023).

92. Przybylińska, H., Hendorfer, G., Bruckner, M., Palmetshofer, L. & Jantsch, W. On the local structure of optically active er centers in si. *Appl. Phys. Lett.* **66**, 490–492 (1995).
93. Vinh, N., Przybylińska, H., Krasil'nik, Z. & Gregorkiewicz, T. Microscopic structure of er-related optically active centers in crystalline silicon. *Phys. Rev. Lett.* **90**, 066401 (2003).
94. Sutula, M. et al. Large-scale optical characterization of solid-state quantum emitters. *Nat. Mater.* **22**, 1338–1344 (2023).
95. Li, L. et al. Heterogeneous integration of spin-photon interfaces with a scalable CMOS platform. *arXiv* https://arxiv.org/abs/2308.14289 (2023).
96. Dhaliah, D., Xiong, Y. H., Sipahigil, A., Griffin, S. M. & Hautier, G. First-principles study of the t center in silicon. *Phys. Rev. Mater.* **6**, L053201 (2022).
97. DeAbreu, A. et al. Waveguide-integrated silicon t centres. *Opt. Express* **31**, 15045–15057 (2023).
98. Kobayashi, T. et al. Engineering long spin coherence times of spin-orbit qubits in silicon. *Nat. Mater.* **20**, 38–42 (2021).
99. Yin, C. M. et al. Optical addressing of an individual erbium ion in silicon. *Nature* **497**, 91–94 (2013).
100. Palm, J., Gan, F., Zheng, B., Michel, J. & Kimerling, L. C. Electroluminescence of erbium-doped silicon. *Phys. Rev. B* **54**, 17603–17615 (1996).
101. Taguchi, A., Takahei, K., Matsuoka, M. & Tohno, S. Evaluation of the energy-transfer rate between an er 4f shell and a si host in er-doped si. *J. Appl. Phys.* **84**, 4471–4478 (1998).
102. Priolo, F., Franzo, G., Coffa, S. & Carnera, A. Excitation and nonradiative deexcitation processes of er3+ in crystalline si. *Phys. Rev. B* **57**, 4443–4455 (1998).
103. Gritsch, A., Ulanowski, A., Pforr, J. & Reiserer, A. Optical single-shot readout of spin qubits in silicon. *Nat. Commun.* **16**, 64 (2025).

Acknowledgements

The SSPD fabrication is performed at the NSW Node and ACT Node of the NCRIS-enabled Australian National Fabrication Facility. We acknowledge access to NCRIS funded facilities and expertise at the ion-implantation Laboratory (iiLab), a node of the Heavy Ion Accelerator (HIA) Capability at the Australian National University. This work is supported by the ARC Centre of Excellence for Quantum Computation and Communication Technology (Grant CE170100012) and the Discovery Project (Grant DP210101784). We thank Prof. M. L. W. Thewalt for providing us the ^{28}Si wafer and we thank Dr. Sae Woo Nam for kind support to establish the SSPD fabrication process at the University of New South Wales, Sydney.

Author contributions

I.R.B. and A.L. conducted the experiments and performed the data processing. I.R.B., A.L., G.G.d.B., J.G.B., B.C.J., J.C.M., R.L.A., M.J.S., C.Y. and S.R. contributed to the data analysis. S.Q.L., B.C.J. and J.C.M. carried out the Er implantation. N.V.A. and H.-J.P. provided the ^{28}Si samples. I.R.B., B.-B.X. and S.X. contributed to the fabrication and characterization of the SNSPDs. M.J.S. and S.R. conceived the project. S.R. supervised the project. All authors contributed to the writing of the manuscript.

Competing interests

The authors declare no competing interests.

Additional information

Supplementary information The online version contains supplementary material available at https://doi.org/10.1038/s41534-025-01008-x.

Correspondence and requests for materials should be addressed to Sven Rogge.